



Article

Premade Nanoparticle Films for the Synthesis of Vertically Aligned Carbon Nanotubes

Abdul Hoque¹ , Ahamed Ullah² , Beth S. Guiton² and Noe T. Alvarez^{1,*}

¹ Department of Chemistry, University of Cincinnati, Cincinnati, OH 45221, USA; hoqueml@mail.uc.edu

² Department of Chemistry, University of Kentucky, Lexington, KY 40506, USA; ahamed.ullah@uky.edu (A.U.); beth.guiton@uky.edu (B.S.G.)

* Correspondence: noe.alvarez@uc.edu

Abstract: Carbon nanotubes (CNTs) offer unique properties that have the potential to address multiple issues in industry and material sciences. Although many synthesis methods have been developed, it remains difficult to control CNT characteristics. Here, with the goal of achieving such control, we report a bottom-up process for CNT synthesis in which monolayers of premade aluminum oxide (Al₂O₃) and iron oxide (Fe₃O₄) nanoparticles were anchored on a flat silicon oxide (SiO₂) substrate. The nanoparticle dispersion and monolayer assembly of the oleic-acid-stabilized Al₂O₃ nanoparticles were achieved using 11-phosphonoundecanoic acid as a bifunctional linker, with the phosphonate group binding to the SiO₂ substrate and the terminal carboxylate group binding to the nanoparticles. Subsequently, an Fe₃O₄ monolayer was formed over the Al₂O₃ layer using the same approach. The assembled Al₂O₃ and Fe₃O₄ nanoparticle monolayers acted as a catalyst support and catalyst, respectively, for the growth of vertically aligned CNTs. The CNTs were successfully synthesized using a conventional atmospheric pressure-chemical vapor deposition method with acetylene as the carbon precursor. Thus, these nanoparticle films provide a facile and inexpensive approach for producing homogenous CNTs.



Citation: Hoque, A.; Ullah, A.; Guiton, B.S.; Alvarez, N.T. Premade Nanoparticle Films for the Synthesis of Vertically Aligned Carbon Nanotubes. *C* **2021**, *7*, 79. <https://doi.org/10.3390/c7040079>

Academic Editor: Gil Goncalves

Received: 11 October 2021

Accepted: 16 November 2021

Published: 19 November 2021

Publisher's Note: MDPI stays neutral with regard to jurisdictional claims in published maps and institutional affiliations.



Copyright: © 2021 by the authors. Licensee MDPI, Basel, Switzerland. This article is an open access article distributed under the terms and conditions of the Creative Commons Attribution (CC BY) license (<https://creativecommons.org/licenses/by/4.0/>).

Keywords: vertically aligned carbon nanotubes; catalyst; catalyst support; nanoparticles; monolayer

1. Introduction

The synthesis of vertically aligned carbon nanotubes (VA-CNTs) on a planar substrate has been established as a method for growing high-quality CNTs with controlled lengths [1,2]. Conventional CNT synthesis by chemical vapor deposition (CVD) requires a catalyst-support film of aluminum oxide (Al₂O₃) and an active metal catalyst. Furthermore, the interactions between the catalyst and catalyst support are crucial for enhancing the catalyst lifetime and VA-CNT growth [3–5]. Such catalysts are commonly prepared using traditional top-down methods, with films being deposited using physical processes such as e-beam deposition, sputtering, or atomic layer deposition. Unfortunately, these catalysts provide little control over the type of CNTs that are produced, or their diameters, which is largely due to the catalyst and catalyst support preparation method. Typically, a thin film of Al₂O₃ (~10 nm) is deposited as a catalyst support followed by the deposition of a thin catalyst film (0.5–3 nm of Fe) [6,7]. Upon exposure to a high temperature and reduction, the catalyst layer forms densely packed islands, which act as nucleation sites for CNT growth [8]. As a result, it is nearly impossible to control the catalyst nanoparticle size, and consequently, to calculate the CNT diameter ahead of time, as the nanoparticle size generally determines the nanotube diameter [9–11]. In addition, these techniques typically require expensive instrumentation, which may have a significant impact on the large-scale production of CNTs.

The development of less expensive and well-controlled methods for depositing catalysts and catalyst supports has generated considerable research interest. Although controlling the catalyst nanoparticle size is expected to provide control over the CNT diameter,

the preparation of monodisperse catalyst nanoparticles and their assembly into thin films is challenging, and few methods have been reported [12]. Premade catalyst nanoparticles with controlled densities and sizes can affect the number of nucleation sites and the CNT diameters, respectively [13]. Efforts in this field have demonstrated the effective growth of VA-CNT arrays [14,15], but a greater control over particle size and the build-up of catalyst monolayer films is required. Investigations of individual catalyst nanoparticles can be used to elucidate their characteristics and their catalytic activity toward CNT growth. The lower temperatures that are required for nanoparticle synthesis should favor diameter control. Moreover, wet chemistry methods for catalyst and catalyst support deposition for CNT synthesis should be less expensive than traditional physical evaporation methods.

The deposition of catalyst nanoparticles on a substrate by drop casting has a limited ability to provide uniform monolayer films [16]. In contrast, the assembly of a uniform nanoparticle monolayer on a chemically functionalized substrate is a suitable technique [14,17,18]. An Al_2O_3 catalyst support layer consisting of premade nanoparticles can prevent catalyst diffusion [19] and increase hydrocarbon decomposition [20]. However, there are many challenges associated with assembling nanoparticles in solution into a continuous thin film, including particle diameter uniformity (monodispersity) and the packing of nanoparticles into high-density two-dimensional films while avoiding the formation of double or multiple layers. The assembly of nanoparticle monolayers on planar substrates has been explored using crosslinking agents as anchoring groups [21–24]. (3-Aminopropyl)triethoxysilane has been applied as an intermediate ligand for the formation of monolayers of nanoparticles with amino ($-\text{NH}_2$) groups, which can bind with or replace other organic functional groups [25,26]. Monolayers of iron oxide (Fe_3O_4) nanoparticles on glass plates were successfully assembled using a hydroxypropyl cellulose (HPC) biopolymer thin film, with the HPC intermediate linkers forming hydrogen bonds with both the substrate and nanoparticle surfaces [27]. Therefore, it is understood that nanoparticle assembly as a monolayer depends on the organic or inorganic coating on the nanoparticle surface and the chemical nature of the substrate.

Oleic acid is a carboxylate-containing long-chain organic molecule that is used as a surface stabilizing agent for nanoparticle synthesis [28]. Al_2O_3 or Fe_3O_4 nanoparticles coated with oleic acid can be assembled into a monolayer on a substrate by using organic linker molecules. Bifunctional 11-phosphonoundecanoic acid (PNDA) is a suitable linker that can bind to a metal oxide substrate via its phosphonate group to form a carboxylic acid thin film [21,29]. The carboxylate groups in both oleic acid (on the nanoparticle surfaces) and PNDA (on the metal oxide substrate) can undergo ligand exchange reactions in solution. Chemically bonded carboxylate groups on Fe_3O_4 nanoparticles can facilitate the formation of a uniform monolayer of catalyst particles on a substrate. Monolayer formation on a substrate that is modified with an organic ligand can increase both the uniformity and particle density on the substrate. These features are advantageous, as it has been reported that a high density of catalyst particles is required to grow VA-CNTs [30,31].

Here, we report the bottom-up assembly of premade nanoparticle monolayer films of Al_2O_3 and Fe_3O_4 for the synthesis of VA-CNTs. Using spherical nanoparticles that were synthesized in solution, Al_2O_3 and Fe_3O_4 monolayers were sequentially assembled on an SiO_2 substrate. Nanoparticle separation was performed in order to enhance the homogeneity of the assembled monolayer films. The obtained nanoparticle films were then successfully applied to catalyze the growth of VA-CNTs.

2. Experimental

Materials: Aluminum chloride (Reagents Plus, $\geq 99\%$), iron (III) chloride hexahydrate (reagent grade, $\geq 98\%$), 1-octadecene (technical grade, $\geq 90\%$), oleic acid (technical grade, $\geq 90\%$), and PNDA ($\geq 90\%$) were purchased from Sigma-Aldrich (St. Louis, MO, USA) and used without further purification. Sodium oleate ($\geq 97.0\%$) was purchased from TCI Chemicals. 1-Hexadecene (technical grade, $\geq 92\%$), hexane (ACS grade, $\geq 99.5\%$), and ethanol (ACS grade) were purchased from Fischer Scientific. Silicon wafers with

500 nm \pm 5% thermal oxide layer on top surface were purchased from University Wafer (South Boston, MA, USA). Ultrathin carbon type-A 400 mesh copper grids with lacey carbon for transmission electron microscopy (TEM) characterization were obtained from Ted Pella (Redding, CA, USA).

Characterization: Fourier transform infrared (FTIR) spectroscopy was used to analyze the aluminum oleate and iron oleate precursors as well as the synthesized nanoparticles. The sizes and shapes of the Al₂O₃ and Fe₃O₄ nanoparticles were characterized by atomic force microscopy (AFM; Bruker Dimension icon ScanAsyst AFM, Billerica, MA, USA), TEM (JEOL JEM-1230, Tokyo, Japan), and scanning electron microscopy (Philips FEI XL30 ESEM, North Billerica, MA, USA). X-ray photoelectron spectroscopy (XPS; K-Alpha, Thermo Scientific, Waltham, MA, USA) using a 400 μ m spot area was used to investigate the presence of linker molecules on metal oxide substrates. Raman spectroscopy using an inVia confocal Raman microscope (Renishaw, Gloucestershire, UK) with a 633 nm laser at 10% power was used to evaluate the quality of the grown nanotubes.

Al₂O₃ nanoparticle synthesis: Al₂O₃ nanoparticles were synthesized by the thermal decomposition of an aluminum oleate precursor in 1-octadecene as a high-boiling solvent. The aluminum oleate precursor was prepared by reacting AlCl₃ (5 g) and sodium oleate (20 g) in a solvent mixture (70 mL hexane + 40 mL ethanol + 30 mL H₂O) for 4 h under reflux at 70 °C with continuous stirring [32]. Subsequently, 1.5 g (1.7 mmol) of aluminum oleate and 1.5 mL of oleic acid (as a capping agent) were dissolved in 50 mL of 1-octadecene. Using a three-neck boiling flask, this mixture was heated to 320 °C for 2 h with continuous stirring. When the temperature was close to 320 °C, continuous bubbling was observed and the transparent solution became creamy white, indicating the nucleation of Al₂O₃ nanoparticles. After cooling to ambient temperature, the Al₂O₃ nanoparticles were precipitated using a 1:1 mixture of isopropyl alcohol and hexane. Subsequently, Al₂O₃ nanoparticles of different sizes were separated by centrifugation. The large-size oleic-acid-stabilized Al₂O₃ nanoparticles were first separated by centrifugation at 8000 rpm for 60 min, and then smaller Al₂O₃ nanoparticles were separated at 12,000 and 15,000 rpm for 60 min. The Al₂O₃ nanoparticles were then redispersed in hexane or a hexane/isopropyl alcohol mixture (1:1) for further use.

Fe₃O₄ nanoparticle synthesis: Fe₃O₄ nanoparticles with uniform sizes were synthesized from an iron oleate precursor according to the procedure reported by Park et al. with some modifications [33]. Iron oleate (1.5 g, 1.67 mmol) and oleic acid (1.5 mL) were dissolved in 1-hexadecene (50 mL). Using a three-neck boiling flask, the mixture was heated at 284 °C for 60 min with continuous stirring under a nitrogen flow to control oxidation. The black solution was cooled to ambient temperature and 50 mL of ethanol was added to precipitate the Fe₃O₄ nanoparticles. Then, Fe₃O₄ nanoparticles of different sizes were separated by centrifugation and redispersed in hexane for further use [12,34].

Formation of Al₂O₃ nanoparticle monolayer: One side polished SiO₂ layer (500 nm \pm 5%) on one side of the silicon wafer was employed as a substrate for the synthesis of VA-CNTs. In order to form a monolayer of Al₂O₃ nanoparticles, the SiO₂ substrate was modified with bifunctional PNDA using the procedure reported by Hanson et al. with some modifications [35]. A 3 mm \times 3 mm piece of one-side-polished SiO₂ was cleaned by ultrasonication in acetone for 20 min. The substrate was dried under a nitrogen flow and treated with piranha solution (H₂SO₄/H₂O₂, 3:1) for 30 min to generate hydroxyl groups on the surface [26,35]. After washing with water and drying under a nitrogen flow, the hydroxylated substrate was immersed in a solution of 2 mM PNDA in ethanol/water (1:1, v/v) for 48 h to attach PNDA ligands to the surface. The substrate was washed with ethanol and an ethanol/water mixture (50:50). Subsequently, the substrate was immersed in a 3 mg/mL solution of oleic-acid-coated Al₂O₃ nanoparticles for 3 h to initiate a ligand exchange reaction between the terminal carboxylate group of PNDA and the carboxylate group of the oleic acid on the Al₂O₃ nanoparticle surface, thus forming a nanoparticle monolayer. Any physisorbed particles were removed from the substrate surface by washing with hexane.

Formation of Fe₃O₄ nanoparticle monolayer: An Fe₃O₄ nanoparticle monolayer was formed on the Al₂O₃ nanoparticle layer using a similar procedure [21]. The substrate with the Al₂O₃ nanoparticle monolayer was annealed at 700 °C for 2 h to remove all of the organic ligands from the surface and to convert any aluminum hydroxide to Al₂O₃. Then, the substrate was treated with piranha solution and immersed in a 2 mM PNDA solution to bind the linker molecules for the Fe₃O₄ monolayer formation. The substrate was immersed in an Fe₃O₄ nanoparticle solution to promote the ligand exchange reaction between the terminal carboxylate group of PNDA and the carboxylate group of oleic acid on the Fe₃O₄ nanoparticle surface. Optimized conditions (3 mg/mL Fe₃O₄ nanoparticle solution for 3 h) gave a compact monolayer of Fe₃O₄ nanoparticles. To remove any physisorbed particles from the surface, the substrate was washed with hexane. The substrate was then heated at 400 °C for 1 h to remove the oleic acid capping agent and any other organics from the surface.

CNT synthesis: The CNTs were synthesized on the substrate with premade Al₂O₃ and Fe₃O₄ nanoparticle monolayers using CVD. Initially, the substrate was heated at 450 °C for 15 min in the presence of hydrogen in order to thermally reduce the Fe₃O₄ catalyst nanoparticles to metallic iron. Then, VA-CNTs were grown by CVD at 750 °C and atmospheric pressure for 20 min using acetylene as the carbon source with argon as the carrier gas.

3. Results and Discussion

The key aspect of this work was the monolayer assembly of premade Fe₃O₄ catalyst and Al₂O₃ catalyst support nanoparticles for the synthesis of VA-CNTs. It has been reported that the synthesis of CNTs with a specific chirality mostly depends on the interactions between the metal catalyst, catalyst support, and hydrocarbon [36–38]. Figure 1A shows a schematic diagram of the process for assembling the catalyst support and catalyst films for VA-CNT growth. Since Al₂O₃ is a common catalyst support for the large-scale synthesis of VA-CNTs, an Al₂O₃ film was prepared on the SiO₂ surface by using premade Al₂O₃ nanoparticles in solution. The formation of the catalyst support monolayer required the SiO₂ substrate to be activated by introducing hydroxyl groups that could be coupled with linker molecules. Subsequently, the SiO₂ substrate was modified with PNDA as an organic linker for binding nanoparticles. Organophosphonic acids have been widely used as ligands for metal oxide (e.g., SiO₂ and Al₂O₃) functionalization in various applications, with the phosphonate group binding to the metal oxide substrate [39–42]. A similar approach using bifunctional PNDA to form a monolayer of iron–platinum bimetallic nanoparticles on an Al₂O₃ substrate indicated that the phosphonate and –COOH groups of PNDA were bound to the Al₂O₃ substrate and the nanoparticle surface, respectively [21]. The sequential formation of Al₂O₃ and Fe₃O₄ nanoparticle monolayers on the functionalized SiO₂ substrate are shown in Figure 1B,C. Oleic acid on the nanoparticle surfaces facilitated the ligand exchange reaction using –COOH as an anchoring group [43].

The oleic-acid-coated Al₂O₃ nanoparticles that were synthesized from the aluminum oleate precursor were spherical, as shown in Figure S1. Larger Al₂O₃ nanoparticles were separated as the decant by centrifugation at 12,000 rpm for 60 min (Figure S1A), whereas comparatively small Al₂O₃ nanoparticles remained in the decanted solution (Figure S1B), which were chosen to form the monolayer on the SiO₂ substrate. FTIR spectroscopy was used to confirm the presence of an oleic acid coating on the surface of the Al₂O₃ nanoparticles (Figure S2). Characteristic bands associated with –CH₂, –CH, and C=O groups were observed for oleic acid (Figure S2A), aluminum oleate (Figure S2B), and the oleic-acid-coated Al₂O₃ nanoparticles (Figure S2C). The strong band at 1595 cm^{−1} in the FTIR spectrum of aluminum oleate (Figure S2B) corresponded to a COO–Al species [32], which is typically found at 1600 cm^{−1} [44]. The FTIR spectrum of oleic-acid-capped Al₂O₃ (Figure S2C) showed C–H stretching peaks but no carbonyl peak. The strong peak at ~1465 cm^{−1} and the peak at ~1600 cm^{−1} (Figure S2C), which are characteristic of symmetric and asymmetric carboxylate (COO[−]) stretching, indicated that oleic acid was bound to the

Al_2O_3 nanoparticle surface [45]. In addition, the appearance of a strong $-\text{OH}$ stretching band at $3000\text{--}3600\text{ cm}^{-1}$ (Figure S2C) suggested the presence of hydroxylated Al_2O_3 particles. The FTIR spectrum of the Al_2O_3 nanoparticles that were annealed at $700\text{ }^\circ\text{C}$ (Figure S2D) indicated that all of the organic functional groups, including oleic acid, were removed from the surface.

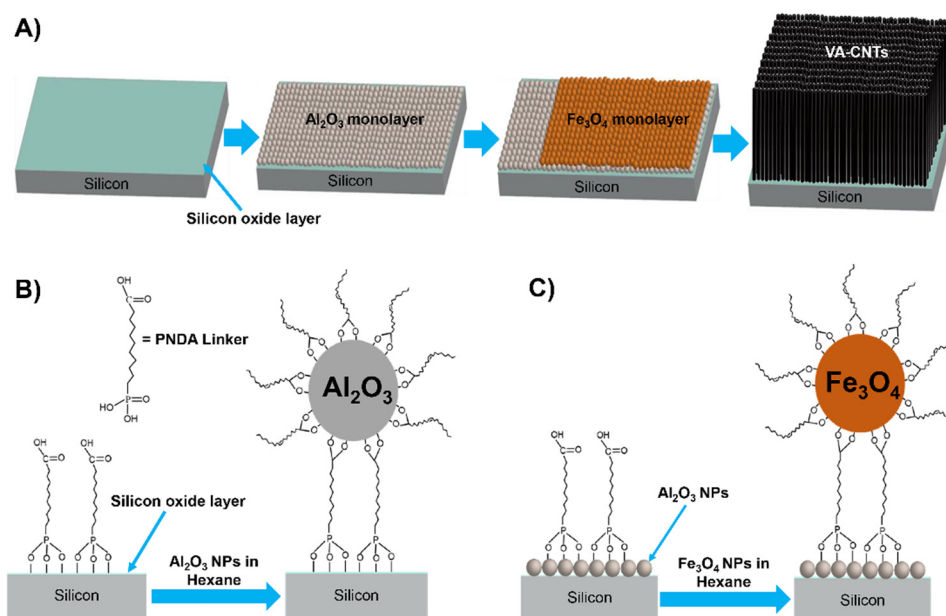


Figure 1. Schematic illustration of catalyst support and catalyst nanoparticle monolayer film assembly for the synthesis of VA-CNTs. (A) Step-wise formation of Al_2O_3 and Fe_3O_4 nanoparticle monolayers on a freshly cleaned SiO_2 wafer. Schematic representations of (B) Al_2O_3 and (C) Fe_3O_4 nanoparticle monolayer assembly.

The sizes and shapes of the Al_2O_3 nanoparticles were characterized using AFM and TEM (Figure 2). Figure 2A shows an AFM image of the Al_2O_3 nanoparticles that were used for monolayer assembly as a catalyst support for VA-CNT growth. As shown by the particle size distribution (Figure 2B), the separated Al_2O_3 nanoparticles had an average size of $6.2 \pm 1.4\text{ nm}$. TEM characterization of the Al_2O_3 nanoparticles was performed before and after annealing (Figure 2C,D). TEM imaging of the oleic-acid-coated Al_2O_3 nanoparticles before annealing was difficult, likely because the organic coating or the hydroxylated nature of the nanoparticles interfered with the electron beam contrast. For the Al_2O_3 nanoparticles before annealing, the TEM sample was prepared by drop casting the nanoparticle solution on the TEM grid and subsequently baking the grid for 2 days at $70\text{ }^\circ\text{C}$. As shown in Figure 2C, the Al_2O_3 nanoparticles before annealing were well distributed. For the Al_2O_3 nanoparticles after annealing at $700\text{ }^\circ\text{C}$ for 2 h, the nanoparticles were dispersed in isopropyl alcohol, the large Al_2O_3 nanoparticle aggregates were separated by centrifugation, and a few drops of Al_2O_3 nanoparticle solution were drop cast onto a copper grid for TEM characterization. As shown in Figure 2D, the Al_2O_3 nanoparticles, after annealing, showed some aggregation and distortion. XPS analysis was performed in order to confirm the elemental state of aluminum in the nanoparticles. Figure S3 shows the $\text{Al}2\text{p}$ and $\text{O}1\text{s}$ core-level spectra. The $\text{Al}2\text{p}$ peak at a binding energy of 74.3 eV is consistent with the presence of Al_2O_3 in the nanoparticles [46]. The deconvoluted $\text{O}1\text{s}$ peaks at 531 and 532.6 eV indicated the presence of two different types of oxygen. The peak at 531 eV corresponded to Al_2O_3 , whereas the peak at 532.6 eV could be due to dissolved oxygen (moisture) or hydroxyl groups in the sample [47,48]. Although these results indicate a high content of surface $-\text{OH}$ groups on the Al_2O_3 nanoparticles, the high temperature used for CVD will convert them into oxides during the CNT synthesis process.

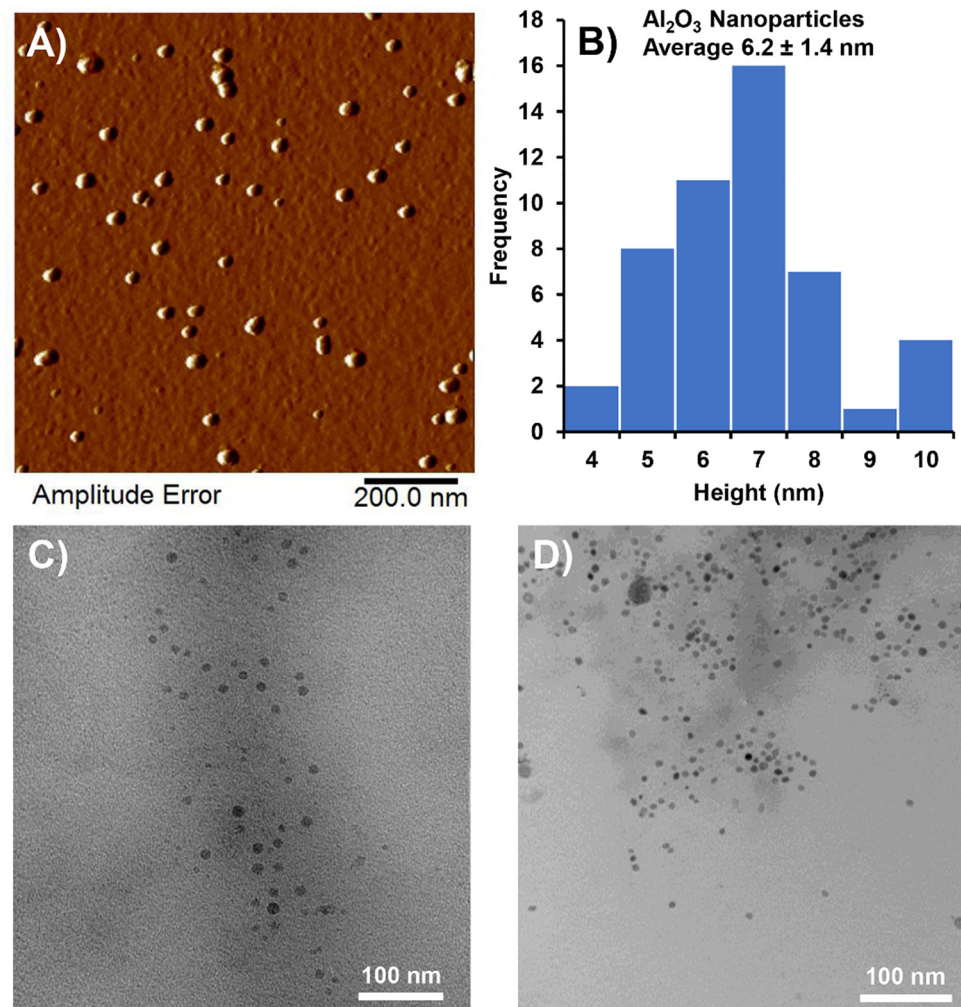


Figure 2. Characterization of synthesized Al_2O_3 nanoparticles. (A) AFM image of Al_2O_3 nanoparticles, (B) Al_2O_3 nanoparticle size distribution, (C) TEM image of Al_2O_3 nanoparticles before annealing, and (D) TEM image of Al_2O_3 nanoparticles after annealing at 700°C .

Fe_3O_4 nanoparticles were synthesized using iron oleate as a precursor and 1-hexadecene as a solvent, similar to the method reported by Park et al. [33]. The obtained oleic-acid-stabilized Fe_3O_4 nanoparticles of different sizes were separated by centrifugation at various speeds. After removing the larger particles, the precipitate that was obtained at 8000 rpm gave a relatively homogenous size distribution, as shown by the AFM image in Figure 3A and the corresponding particle size distribution in Figure 3B. The Fe_3O_4 catalyst nanoparticles with an average size of 9.3 ± 1.2 nm were chosen to form a monolayer on the Al_2O_3 film for VA-CNT growth. The low- and high-magnification TEM images in Figure 3C,D reveal that these Fe_3O_4 nanoparticles had relatively uniform sizes and shapes. FTIR spectral analysis was used to verify the presence of an oleic acid coating on the nanoparticle surface. As shown in Figure S4, the FTIR spectra of oleic acid, iron oleate, and the oleic-acid-coated Fe_3O_4 nanoparticles contained characteristic bands associated with $-\text{CH}_2$, $-\text{CH}$, and $\text{C}=\text{O}$ groups. The characteristic asymmetric and symmetric $\text{COO}-\text{Al}$ bands at ~ 1438 and ~ 1600 cm^{-1} (Figure S4B) confirm the prepared aluminum oleate precursor for the synthesis of Fe_3O_4 catalyst nanoparticles. For the oleic-acid-coated Fe_3O_4 nanoparticles, a strong $\text{C}-\text{H}$ stretching band appeared at ~ 2850 cm^{-1} , but the intensity of the carbonyl stretching band at 1710 cm^{-1} was reduced (Figure S4C). The characteristic asymmetric and symmetric stretching bands at ~ 1438 and ~ 1600 cm^{-1} (Figure S4C), respectively, confirmed that oleic acid was chemisorbed on the Fe_3O_4 nanoparticles [49]. Although the Fe_3O_4 nanoparticles

contained both $\gamma\text{-Fe}_2\text{O}_3$ and Fe_3O_4 , the dominant phase was Fe_3O_4 based on the synthetic method that was used [33]. The liquid-phase synthesis of the catalyst nanoparticles provides direct control over particle size because oleic acid acts as a passivation layer to reduce nanoparticle aggregation [50]. In wet chemical processes, an oxygen-free environment and low synthesis temperature reduce the size of the obtained nanoparticles, whereas catalyst formation at high temperatures provides less control over particle size.

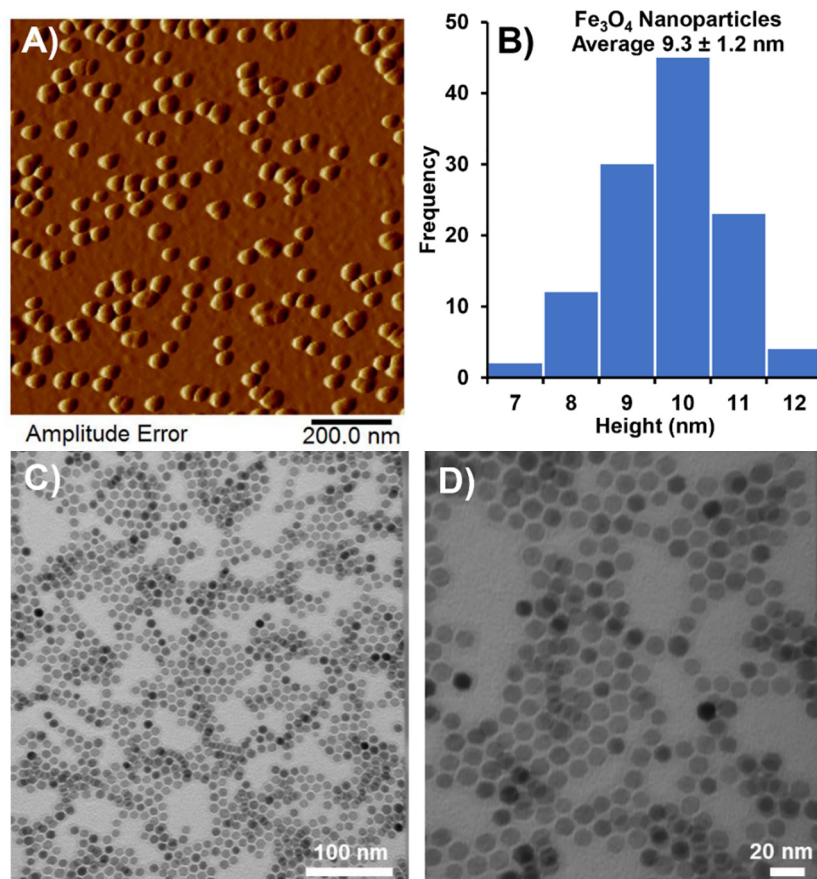


Figure 3. Characterization of synthesized Fe_3O_4 nanoparticles. (A) AFM image of Fe_3O_4 nanoparticles, (B) Fe_3O_4 nanoparticle size distribution, (C) low-magnification TEM image of Fe_3O_4 nanoparticles, and (D) high-magnification TEM image of Fe_3O_4 nanoparticles.

The use of catalyst nanoparticle dispersions with uniform sizes for the assembly of monolayer films could provide improved control over CNT characteristics. Importantly, as this approach is less expensive than traditional catalyst preparation processes, scalable VA-CNT growth can be realized. Bifunctional or multifunctional molecules can be employed as linkers on substrates/surfaces depending on the strength of the interaction between the functional group and substrate. Surface hydroxyl ($-\text{OH}$) groups on SiO_2 and Al_2O_3 generated by piranha treatment can enhance the reactivity toward linker molecules [51]. The condensation reaction between the hydroxyl group of a silanol and the phosphonic acid group of PNDA produced a phosphonate group that was bound to the substrate surface and H_2O as a byproduct [35,52]. Phosphonate groups have a higher grafting rate and stronger binding ability with metal oxide substrates than carboxylate groups [53]. The XPS analysis was conducted to confirm the functionalization of silicon oxide substrate with PNDA ligand. Figures S5 and S6 show the XPS survey spectra of the bare SiO_2 substrate and the SiO_2 substrate with bound phosphonate groups (PNDA), which were compared to reference XPS spectra [54]. The core-level $\text{Si}2\text{p}$, $\text{P}2\text{p}$, $\text{O}1\text{s}$, and $\text{C}1\text{s}$ spectra are shown in Figure S7. The $\text{P}2\text{p}$ peak at a binding energy of 132.9 eV confirmed the successful binding of phosphonate to the SiO_2 substrate.

An Al_2O_3 nanoparticle monolayer was formed on the PNDA-functionalized SiO_2 substrate via a ligand exchange reaction in an Al_2O_3 nanoparticle solution. The carboxylate (COOH) group of the PNDA linker on the SiO_2 substrate was exchanged with the COOH group of oleic acid on the Al_2O_3 nanoparticle surface [21]. After the successful Al_2O_3 monolayer formation, the substrate was dried at 400°C for 1 h and characterized by AFM in tapping mode (Figure 4). The surface morphology of the bare SiO_2 substrate (Figure 4A) was very smooth with no particles, whereas the Al_2O_3 nanoparticle assembly (Figure 4B) exhibited well-distributed nanoparticles on the surface. The cross-sectional profile of the bare SiO_2 substrate (Figure 4C) showed that the substrate was almost planar with a height variation of ~ 0.5 nm. In contrast, the cross-sectional profile of the Al_2O_3 nanoparticle assembly (Figure 4D) showed a nanoparticle layer with a height variation of ~ 5 nm, which is similar to the average size of the Al_2O_3 nanoparticles that were used for monolayer formation. Thus, the liquid-phase preparation of an Al_2O_3 catalyst support via monolayer assembly is suitable for the development of an easy and inexpensive method for the large-scale synthesis of VA-CNTs. The Al_2O_3 film was annealed at 700°C for 2 h to remove all of the organic molecules (capping agents and surface ligands) from the surface and convert any aluminum hydroxide to the oxide for application as a catalyst support.

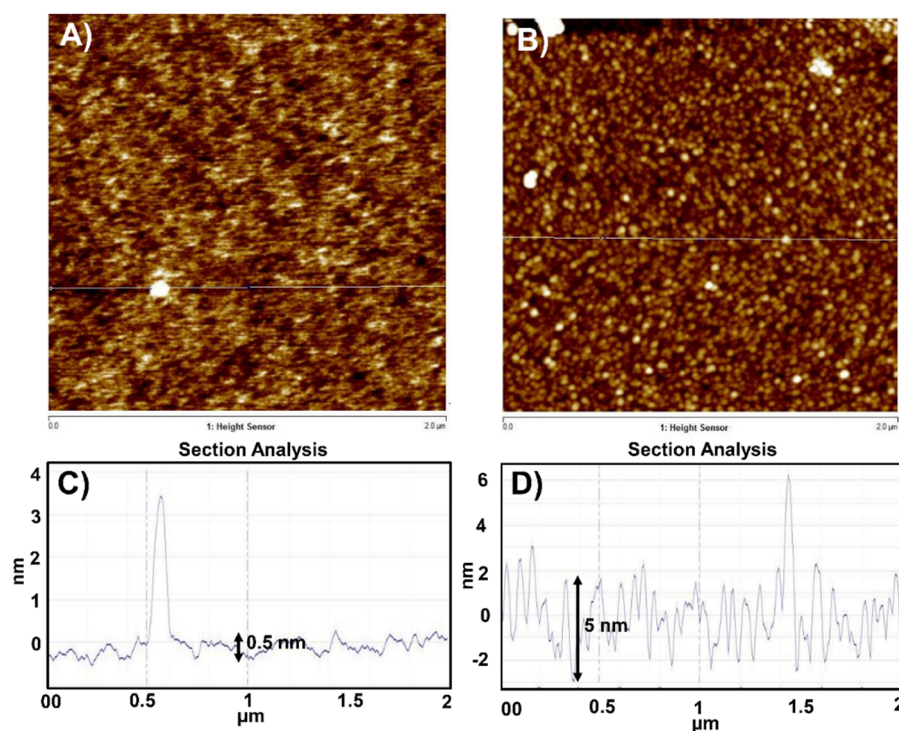


Figure 4. Surface morphology of the SiO_2 substrate before and after assembly of the Al_2O_3 nanoparticle monolayer. AFM images of (A) the bare SiO_2 substrate and (B) the Al_2O_3 nanoparticle monolayer. Height cross-sectional profiles (surface roughness) of (C) the bare SiO_2 substrate and (D) the Al_2O_3 nanoparticle monolayer.

Al_2O_3 interacts strongly with iron, which can reduce the aggregation of catalyst particles on the substrate. Thus, an Fe_3O_4 monolayer was formed over the Al_2O_3 layer, which was modified with PNDA using a procedure similar to that for the SiO_2 substrate. The successful binding of PNDA on the Al_2O_3 monolayer was confirmed by XPS. The XPS survey spectrum of the PNDA film on the Al_2O_3 layer (Figure S8) showed all the core-level peaks of Al_2O_3 as well as a phosphorous peak. The $\text{Al}2p$, $\text{P}2p$, $\text{O}1s$, and $\text{C}1s$ core-level spectra of PNDA on the Al_2O_3 layer are shown in Figure S9. The three peaks in the $\text{C}1s$ spectrum confirmed the presence of carboxylate functionalities on the Al_2O_3 substrate [55]. The $\text{C}1s$ peak at 284.5 eV corresponded to regular carbon (CH , CH_2), whereas the peaks at 285.5 and 289 eV corresponded to carbon in the carbonyl (CO) and

carboxylate (COOH) groups, respectively. A monolayer of Fe_3O_4 catalyst nanoparticles was formed on the Al_2O_3 layer via the ligand exchange reaction between the COOH groups of the PNDA linker on the functionalized Al_2O_3 surface and the COOH group of oleic acid on the Fe_3O_4 nanoparticles in solution. The low- ($15\ \mu\text{m} \times 15\ \mu\text{m}$) and high-magnification AFM images ($2\ \mu\text{m} \times 2\ \mu\text{m}$) of the Fe_3O_4 monolayer (Figure 5A,B) indicated that a compact nanoparticle layer was formed containing nanoparticles of a uniform size. The corresponding cross-sectional profiles of the AFM images (Figure 5C,D) revealed small openings in the monolayer assembly with heights of approximately 10 nm, which is consistent with the average size of the Fe_3O_4 nanoparticles that were used for monolayer formation ($9.3 \pm 1.2\ \text{nm}$). The surface functionalization of metal oxide substrates with monolayers or multilayers of Fe_3O_4 nanoparticles has been studied for various applications [18]. However, Fe_3O_4 nanoparticle monolayers are expected to be suitable as catalysts for VA-CNT growth because the high density and uniformity of catalyst particles can provide control over the number of nanotubes formed in a specific area, as well as their diameters. The density of the Fe_3O_4 nanoparticles on the Al_2O_3 layer was 1.4×10^{11} nanoparticles/ cm^2 , which was determined by counting the nanoparticles using a high-magnification ($100\ \text{nm} \times 100\ \text{nm}$) AFM image. The number of total Fe_3O_4 nanoparticles were manually counted in a $100 \times 100\ \text{nm}^2$ area and their density was extrapolated for a square centimeter area. In addition, the use of a monolayer of uniform catalyst nanoparticles can reduce particle aggregation and catalyst poisoning.

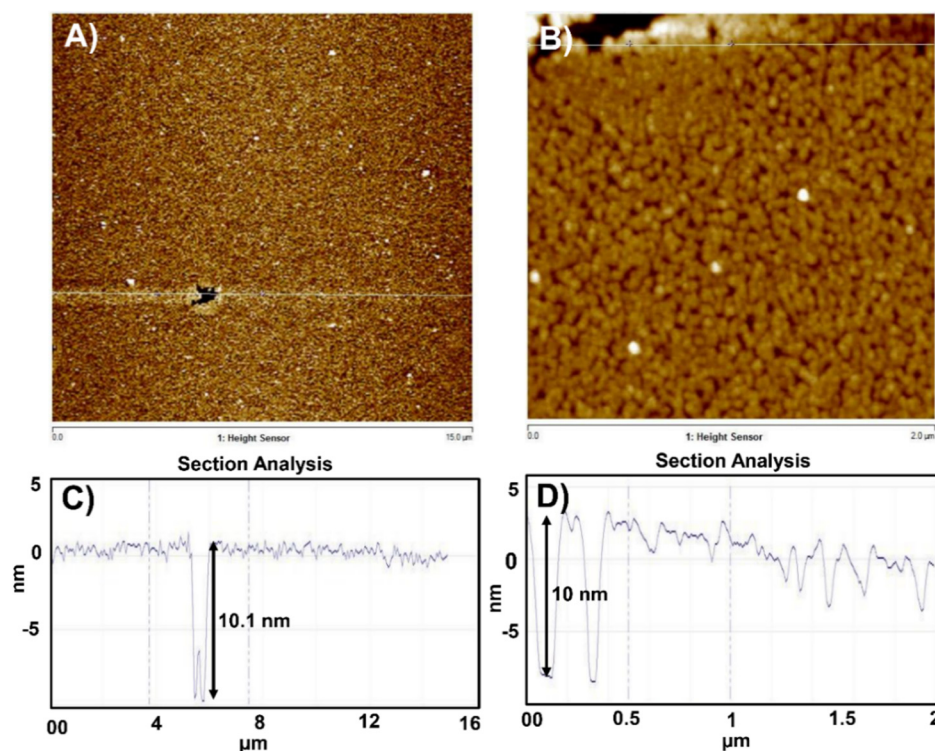


Figure 5. Surface morphology of the Fe_3O_4 nanoparticle monolayer formed over the Al_2O_3 monolayer film. (A) Low-magnification ($15\ \mu\text{m} \times 15\ \mu\text{m}$) and (B) high-magnification ($2\ \mu\text{m} \times 2\ \mu\text{m}$) AFM images of the Fe_3O_4 nanoparticle monolayer. Height cross-sectional profiles corresponding to (C) image A and (D) image B.

Using the premade monolayer of catalyst nanoparticles, CNTs were synthesized by CVD, which is a suitable technique for large-scale synthesis. First, all of the organics were removed from the catalyst surface by heating at $400\ ^\circ\text{C}$ for 2 h in the open air. Subsequently, the Fe_3O_4 monolayer was reduced to metallic iron by thermal reduction at $450\ ^\circ\text{C}$ for 15 min using atomic hydrogen (H) generated from a hydrogen gas (H_2) flow [56]. VA-CNTs were successfully synthesized using acetylene as a carbon precursor at $750\ ^\circ\text{C}$ for

15 min. A comparative literature study about synthesis methods of vertically aligned CNTs from premade nanoparticles is shown in supplementary information (Table S1). The table compares different methodologies used for assembly of catalyst nanoparticles for CNTs growth. Figure 6A,B show low- and high-magnification SEM images of the grown VA-CNTs where uniform-length of CNTs are observed. Though the density of catalyst nanoparticles in Figure 5B is quite very high, the lower density of CNTs growth can be the result of lower nucleation rates of catalyst particles. Authors think that investigating the suitable synthesis parameters in CVD reaction can increase the nucleation rates which can increase the density of VACNTs. TEM imaging (Figure 6C) indicated that the CNTs that were grown from the catalyst nanoparticle monolayer had relatively similar diameters. The quality of the grown CNTs was assessed using Raman spectral analysis (Figure 6D). The characteristic G peak of CNTs, which corresponds to sp^2 carbon, was more prominent than the D peak, which corresponds to sp^3 carbon, indicating the structural defects of CNTs, which are typical of multilayer CNTs. A small RBM peak was also observed in the Raman spectrum of the VA-CNTs, which indicated the presence of a few single-walled CNTs among the mostly multi-walled CNTs.

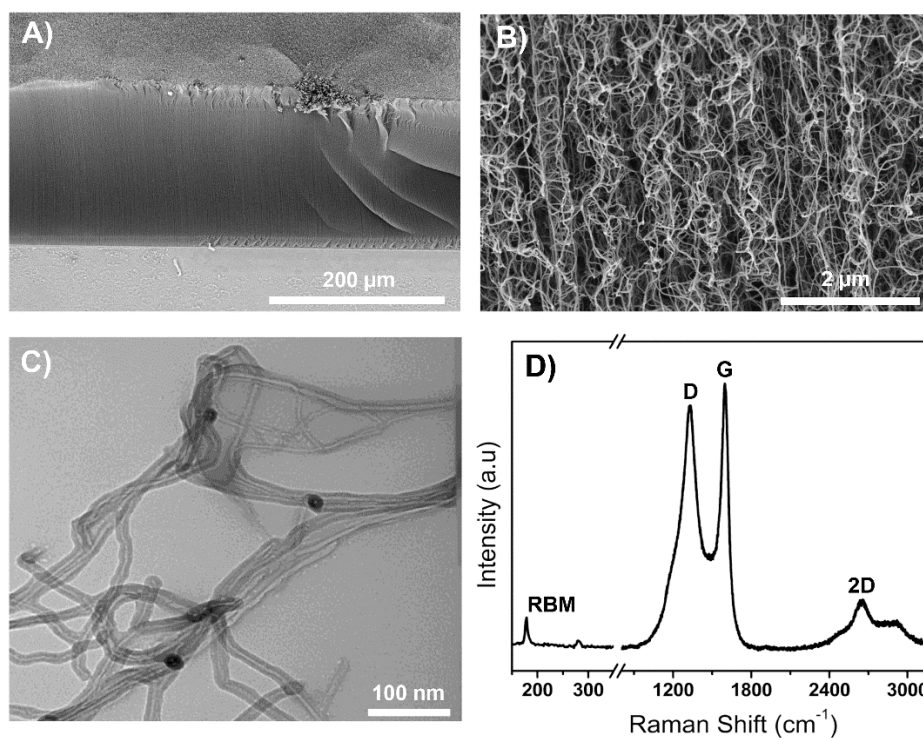


Figure 6. Characterization of VA-CNTs grown from the premade nanoparticle monolayer assembly. (A) Low-magnification SEM image, (B) high-magnification SEM image, (C) high-magnification TEM image, and (D) Raman spectrum of VA-CNTs.

4. Conclusions

Spherical Al_2O_3 and Fe_3O_4 nanoparticles were synthesized and separated into different sizes by varying the centrifugation speed, which provided sufficiently homogenous nanoparticles with which to form monolayer films. Using wet chemical processes, continuous monolayer films of Al_2O_3 nanoparticles as a catalyst support and Fe_3O_4 nanoparticles as a catalyst were sequentially assembled on an SiO_2 substrate using PNDA as a linker molecule. This monolayer assembly was successfully applied to catalyze the growth of uniform, high-density VA-CNTs. This approach for preparing a catalyst support monolayer using premade Al_2O_3 nanoparticles provides an inexpensive and easy alternative to the conventional methods for fabricating thin film catalyst supports such as sputtering, e-beam deposition, and other instrumentation that requires ultrahigh vacuum systems.

Furthermore, the use of a catalyst particle monolayer can improve the homogeneity of the obtained CNTs and increase CNT density.

Supplementary Materials: The following are available online at <https://www.mdpi.com/article/10.3390/c7040079/s1>, Table S1: Current methods of premade catalyst nanoparticles assembly used for CNTs growth; Figure S1: SEM images of spherical shaped aluminum oxide/hydroxide NPs. (A) Large size of aluminum oxide/hydroxide nanoparticles separated by centrifuge technique with 12,000 rpm, (B) Small size of nanoparticles remained in decanted solution. A few drops of nanoparticle solution was drop cast onto a silicon wafer and annealed at 400 °C for an hour before characterization; Figure S2: FTIR spectra of (A) pure oleic acid, (B) aluminum oleate, (C) aluminum oxide nanoparticles without annealing, and (D) aluminum oxide nanoparticles annealed at 700 °C; Figure S3: XPS spectra of aluminum oxide nanoparticles after annealing at 700 °C for 2 h. (A) Survey spectra that represent all the core level peaks, (B) Al 2p, and (C) O 1s; Figure S4: FTIR spectra of (A) pure oleic acid, (B) iron oleate, and (C) oleic acid coated iron oxide nanoparticles; Figure S5: XPS survey spectra of blank silicon oxide substrate that show all the core level peaks; Figure S6: XPS survey spectra of 11-phosphonoundecanoic acid (PNDA) film on silicon substrate showing all core level peaks; Figure S7: XPS spectra of PNDA attached silicon oxide substrate. (A) core level Si 2p peak, (B) core level P 2p peak, (C) core level O 1s peak, and (D) core level C 1s peak; Figure S8: XPS survey spectra of 11-phosphonoundecanoic acid film on alumina monolayer showing all core level peaks; Figure S9: XPS spectra of PNDA attached aluminum oxide substrate. (A) core level Al 2p peak, (B) core level P 2p peak, (C) core level O 1s peak, and (D) core level C 1s peak.

Author Contributions: Conceptualization, methodology, validation, N.T.A. and A.H.; formal analysis, A.H.; investigation, A.H., A.U. and B.S.G.; resources, supervision, project administration, N.T.A.; writing—original draft preparation, A.H.; writing—review and editing, A.H. and N.T.A.; funding acquisition, N.T.A. All authors have read and agreed to the published version of the manuscript.

Funding: This research was funded by NSF, grant number 2016484 under NSF PFI-RP.

Acknowledgments: The authors are thankful for professorship start-up funds from the Department of Chemistry at the University of Cincinnati. Partial salary support for A.U. was provided by an internal seed grant from the University of Kentucky (UK) Energy Research Priority Area program. XPS data were collected at the UK electron microscopy center (EMC), which belongs to the National Science Foundation NNCI Kentucky Multiscale Manufacturing and Nano Integration Node, supported by ECCS-1542174.

Conflicts of Interest: The authors declare no conflict of interest. The funders had no role in the design of the study; in the collection, analyses, or interpretation of data; in the writing of the manuscript, or in the decision to publish the results.

References

1. Alvarez, N.T.; Miller, P.; Haase, M.; Kienzle, N.; Zhang, L.; Schulz, M.J.; Shanov, V. Carbon Nanotube Assembly at Near-Industrial Natural-Fiber Spinning Rates. *Carbon* **2015**, *86*, 350–357. [[CrossRef](#)]
2. Alvarez, N.T.; Miller, P.; Haase, M.R.; Lobo, R.; Malik, R.; Shanov, V. Tailoring Physical Properties of Carbon Nanotube Threads during Assembly. *Carbon* **2019**, *144*, 55–62. [[CrossRef](#)]
3. Amama, P.B.; Pint, C.L.; Kim, S.M.; Eyink, K.G.; Stach, E.A.; Hauge, R.H.; Maruyama, B. Evolution, Activity, and Lifetime of Alumina-Supported Fe Catalyst during Super Growth of Single-Walled Carbon Nanotube Carpets: Influence of the Type of Alumina. *Mater. Res. Soc. Symp. Proc.* **2010**, *1258*, 217–222. [[CrossRef](#)]
4. Modekwe, H.U.; Mamo, M.A.; Moothi, K.; Daramola, M.O. Effect of Different Catalyst Supports on the Quality, Yield and Morphology of Carbon Nanotubes Produced from Waste Polypropylene Plastics. *Catalysts* **2021**, *11*, 692. [[CrossRef](#)]
5. Wang, B.; Yang, Y.; Li, L.J.; Chen, Y. Effect of Different Catalyst Supports on the (n,m) Selective Growth of Single-Walled Carbon Nanotube from Co-Mo Catalyst. *J. Mater. Sci.* **2009**, *44*, 3285–3295. [[CrossRef](#)]
6. Christen, H.M.; Poretzky, A.A.; Cui, H.; Belay, K.; Fleming, P.H.; Geoghegan, D.B.; Lowndes, D.H. Rapid Growth of Long, Vertically Aligned Carbon Nanotubes through Efficient Catalyst Optimization Using Metal Film Gradients. *Nano Lett.* **2004**, *4*, 1939–1942. [[CrossRef](#)]
7. Guzmán De Villoria, R.; Figueredo, S.L.; Hart, A.J.; Steiner, S.A.; Slocum, A.H.; Wardle, B.L. High-Yield Growth of Vertically Aligned Carbon Nanotubes on a Continuously Moving Substrate. *Nanotechnology* **2009**, *20*, 1–8. [[CrossRef](#)]
8. Pint, C.L.; Kim, S.M.; Stach, E.A.; Hauge, R.H. Rapid and Scalable Reduction of Dense Surface-Supported Metal-Oxide Catalyst with Hydrazine Vapor. *ACS Nano* **2009**, *3*, 1897–1905. [[CrossRef](#)]

9. Cheung, C.L.; Kurtz, A.; Park, H.; Lieber, C.M. Diameter-Controlled Synthesis of Carbon Nanotubes. *J. Phys. Chem. B* **2002**, *106*, 2429–2433. [[CrossRef](#)]
10. Kukovitsky, E.F.; L'vov, S.G.; Sainov, N.A.; Shustov, V.A.; Chernozatonskii, L.A. Correlation between Metal Catalyst Particle Size and Carbon Nanotube Growth. *Chem. Phys. Lett.* **2002**, *355*, 497–503. [[CrossRef](#)]
11. Sinnott, S.B.; Andrews, R.; Qian, D.; Rao, A.M.; Mao, Z.; Dickey, E.C.; Derbyshire, F. Model of Carbon Nanotube Growth through Chemical Vapor Deposition. *Chem. Phys. Lett.* **1999**, *315*, 25–30. [[CrossRef](#)]
12. Alvarez, N.T.; Li, F.; Pint, C.L.; Mayo, J.T.; Fisher, E.Z.; Tour, J.M.; Colvin, V.L.; Hauge, R.H. Uniform Large Diameter Carbon Nanotubes in Vertical Arrays from Premade Near-Monodisperse Nanoparticles. *Chem. Mater.* **2011**, *23*, 3466–3475. [[CrossRef](#)]
13. Schäffel, F.; Kramberger, C.; Rümmele, M.H.; Grimm, D.; Mohn, E.; Gemming, T.; Pichler, T.; Rellinghaus, B.; Büchner, B.; Schultz, L. Nanoengineered Catalyst Particles as a Key for Tailor-Made Carbon Nanotubes. *Chem. Mater.* **2007**, *19*, 5006–5009. [[CrossRef](#)]
14. Alvarez, N.T.; Orbaek, A.; Barron, A.R.; Tour, J.M.; Hauge, R.H. Dendrimer-Assisted Self-Assembled Monolayer of Iron Nanoparticles for Vertical Array Carbon Nanotube Growth. *ACS Appl. Mater. Interfaces* **2010**, *2*, 15–18. [[CrossRef](#)]
15. Alvarez, N.T.; Hamilton, C.E.; Pint, C.L.; Orbaek, A.; Yao, J.; Frosinini, A.L.; Barron, A.R.; Tour, J.M.; Hauge, R.H. Wet Catalyst-Support Films for Production of Vertically Aligned Carbon Nanotubes. *ACS Appl. Mater. Interfaces* **2010**, *2*, 1851–1856. [[CrossRef](#)]
16. Yang, Z.; Zhang, S.; Li, L.; Chen, W. Research Progress on Large-Area Perovskite Thin Films and Solar Modules. *J. Mater.* **2017**, *3*, 231–244. [[CrossRef](#)]
17. Chen, J.; Xu, X.; Zhang, L.; Huang, S. Controlling the Diameter of Single-Walled Carbon Nanotubes by Improving the Dispersion of the Uniform Catalyst Nanoparticles on Substrate. *Nano-Micro Lett.* **2015**, *7*, 353–359. [[CrossRef](#)]
18. Pauly, M.; Pichon, B.P.; Albouy, P.A.; Fleutot, S.; Leuvre, C.; Trassin, M.; Gallani, J.L.; Begin-Colin, S. Monolayer and Multilayer Assemblies of Spherically and Cubic-Shaped Iron Oxide Nanoparticles. *J. Mater. Chem.* **2011**, *21*, 16018–16027. [[CrossRef](#)]
19. Amama, P.B.; Pint, C.L.; McJilton, L.; Kim, S.M.; Stach, E.A.; Murray, P.T.; Hauge, R.H.; Maruyama, B. Role of Water in Super Growth of Single-Walled Carbon Nanotube Carpets. *Nano Lett.* **2009**, *9*, 44–49. [[CrossRef](#)]
20. Hasnan, N.S.N.; Timmiati, S.N.; Lim, K.L.; Yaakob, Z.; Kamaruddin, N.H.N.; Teh, L.P. Recent Developments in Methane Decomposition over Heterogeneous Catalysts: An Overview. *Mater. Renew. Sustain. Energy* **2020**, *9*, 1–18. [[CrossRef](#)]
21. Yildirim, O.; Gang, T.; Kinge, S.; Reinhoudt, D.N.; Blank, D.H.A.; van der Wiel, W.G.; Rijnders, G.; Huskens, J. Monolayer-Directed Assembly and Magnetic Properties of FePt Nanoparticles on Patterned Aluminum Oxide. *Int. J. Mol. Sci.* **2010**, *11*, 1162–1179. [[CrossRef](#)] [[PubMed](#)]
22. Andryszewski, T.; Iwan, M.; Hołdyński, M.; Fiałkowski, M. Synthesis of a Free-Standing Monolayer of Covalently Bonded Gold Nanoparticles. *Chem. Mater.* **2016**, *28*, 5304–5313. [[CrossRef](#)]
23. Feichtenschlager, B.; Lomoschitz, C.J.; Kickelbick, G. Tuning the Self-Assembled Monolayer Formation on Nanoparticle Surfaces with Different Curvatures: Investigations on Spherical Silica Particles and Plane-Crystal-Shaped Zirconia Particles. *J. Colloid Interface Sci.* **2011**, *360*, 15–25. [[CrossRef](#)]
24. Tizazu, G. A Simple Method for Patterning Nanoparticles on Planar Surfaces. *J. Nanotechnol.* **2019**, *2019*, 1–7. [[CrossRef](#)]
25. Karade, V.C.; Sharma, A.; Dhavale, R.P.; Dhavale, R.P.; Shingte, S.R.; Patil, P.S.; Kim, J.H.; Zahn, D.R.T.; Chougale, A.D.; Salvan, G.; et al. APTES Monolayer Coverage on Self-Assembled Magnetic Nanospheres for Controlled Release of Anticancer Drug Nintedanib. *Sci. Rep.* **2021**, *11*, 1–12. [[CrossRef](#)]
26. Acres, R.G.; Ellis, A.V.; Alvino, J.; Lenahan, C.E.; Khodakov, D.A.; Metha, G.F.; Andersson, G.G. Molecular Structure of 3-Aminopropyltriethoxysilane Layers Formed on Silanol-Terminated Silicon Surfaces. *J. Phys. Chem. C* **2012**, *116*, 6289–6297. [[CrossRef](#)]
27. Zhou, M.; Hedlund, J. Assembly of Oriented Iron Oxide and Zeolite Crystals via Biopolymer Films. *J. Mater. Chem.* **2012**, *22*, 24877–24881. [[CrossRef](#)]
28. Wah, F.; Mun, L.; Tai, F.; Bee, S.; Hamid, A. Iron Oxide Nanoparticles Decorated Oleic Acid for High Colloidal Stability. *Adv. Polym. Technol.* **2017**, *37*, 1712–1721. [[CrossRef](#)]
29. Tamaki, H.; Abe, S.; Yamagata, S.; Yoshida, Y.; Sato, Y. Self-Assembled Monolayer Formation on a Dental Orthodontic Stainless Steel Wire Surface to Suppress Metal Ion Elution. *Coatings* **2020**, *10*, 367. [[CrossRef](#)]
30. Yamada, K.; Kaneko, A.; Kato, H.; Homma, Y. Vertically-Aligned Carbon Nanotube Growth Using Closely Packed Iron Oxide Nanoparticles. *Mater. Express* **2012**, *2*, 257–260. [[CrossRef](#)]
31. Signore, M.A.; Rizzo, A.; Rossi, R.; Piscopiello, E.; Di Luccio, T.; Capodice, L.; Dikonimos, T.; Giorgi, R. Role of Iron Catalyst Particles Density in the Growth of Forest-like Carbon Nanotubes. *Diam. Relat. Mater.* **2008**, *17*, 1936–1942. [[CrossRef](#)]
32. Lee, D.H.; Condrate, R.A. FTIR Spectral Characterization of Thin Film Coatings of Oleic Acid on Glasses: I. Coatings on Glasses from Ethyl Alcohol. *J. Mater. Sci.* **1999**, *34*, 139–146. [[CrossRef](#)]
33. Park, J.; An, K.; Hwang, Y.; Park, J.E.G.; Noh, H.J.; Kim, J.Y.; Park, J.H.; Hwang, N.M.; Hyeon, T. Ultra-Large-Scale Syntheses of Monodisperse Nanocrystals. *Nat. Mater.* **2004**, *3*, 891–895. [[CrossRef](#)] [[PubMed](#)]
34. Yu, W.W.; Falkner, J.C.; Yavuz, C.T.; Colvin, V.L. Synthesis of Monodisperse Iron Oxide Nanocrystals by Thermal Decomposition of Iron Carboxylate Salts. *Chem. Commun.* **2004**, 2306–2307. [[CrossRef](#)] [[PubMed](#)]
35. Hanson, E.L.; Schwartz, J.; Nickel, B.; Koch, N.; Danisman, M.F. Bonding Self-Assembled, Compact Organophosphonate Monolayers to the Native Oxide Surface of Silicon. *J. Am. Chem. Soc.* **2003**, *125*, 16074–16080. [[CrossRef](#)] [[PubMed](#)]
36. Panic, S.; Bajac, B.; Rakić, S.; Kukovec, K.; Kónya, Z.; Srdić, V.; Boskovic, G. Molybdenum Anchoring Effect in Fe–Mo/MgO Catalyst for Multiwalled Carbon Nanotube Synthesis. *React. Kinet. Mech. Catal.* **2017**, *122*, 775–791. [[CrossRef](#)]

37. He, M.; Zhang, L.; Jiang, H.; Yang, H.; Fossard, F.; Cui, H.; Sun, Z.; Wagner, J.B.; Kauppinen, E.I.; Loiseau, A. FeTiO Based Catalyst for Large-Chiral-Angle Single-Walled Carbon Nanotube Growth. *Carbon* **2016**, *107*, 865–871. [[CrossRef](#)]
38. Harutyunyan, A.R.; Chen, G.; Paronyan, T.M.; Pigos, E.M.; Kuznetsov, O.A.; Hewaparakrama, K.; Kim, S.M.; Zakharov, D.; Stach, E.A.; Sumanasekera, G.U. Preferential Growth of Single-Walled Carbon Nanotubes with Metallic Conductivity. *Science* **2009**, *326*, 116–120. [[CrossRef](#)]
39. Dubey, M.; Weidner, T.; Gamble, L.J.; Castner, D.G. Structure and Order of Phosphonic Acid-Based Self-Assembled Monolayers on Si(100). *Langmuir* **2010**, *26*, 14747–14754. [[CrossRef](#)]
40. Mutin, P.H.; Lafond, V.; Popa, A.F.; Granier, M.; Markey, L.; Dereux, A. Selective Surface Modification of SiO₂-TiO₂ Supports with Phosphonic Acids. *Chem. Mater.* **2004**, *16*, 5670–5675. [[CrossRef](#)]
41. Thissen, P.; Valtiner, M.; Grundmeier, G. Stability of Phosphonic Acid Self-Assembled Monolayers on Amorphous and Single-Crystalline Aluminum Oxide Surfaces in Aqueous Solution. *Langmuir* **2010**, *26*, 156–164. [[CrossRef](#)]
42. Zhao, R.; Rupper, P.; Gaan, S. Recent Development in Phosphonic Acid-Based Organic Coatings on Aluminum. *Coatings* **2017**, *7*, 133. [[CrossRef](#)]
43. Smolensky, E.D.; Park, H.Y.E.; Berquó, T.S.; Pierre, V.C. Surface Functionalization of Magnetic Iron Oxide Nanoparticles for MRI Applications—Effect of Anchoring Group and Ligand Exchange Protocol. *Contrast Media Mol. Imaging* **2011**, *6*, 189–199. [[CrossRef](#)] [[PubMed](#)]
44. Cross, S.N.W.; Rochester, C.H. Infrared Study of the Adsorption of Ethyl Isocyanate on Silica Immersed in Carbon Tetrachloride. *J. Chem. Soc. Faraday Trans. 1 Phys. Chem. Condens. Phases* **1981**, *77*, 1945–1952. [[CrossRef](#)]
45. Lewis, W.K.; Rosenberger, A.T.; Gord, J.R.; Crouse, C.A.; Harruff, B.A.; Fernando, K.A.S.; Smith, M.J.; Phelps, D.K.; Spowart, J.E.; Gulians, E.A.; et al. Multispectroscopic (FTIR, XPS, and TOFMS-TPD) Investigation of the Core-Shell Bonding in Sonochemically Prepared Aluminum Nanoparticles Capped with Oleic Acid. *J. Phys. Chem. C* **2010**, *114*, 6377–6380. [[CrossRef](#)]
46. Van den Brand, J.; Sniijders, P.C.; Sloof, W.G.; Terryn, H.; De Wit, J.H.W. Acid-Base Characterization of Aluminum Oxide Surfaces with XPS. *J. Phys. Chem. B* **2004**, *108*, 6017–6024. [[CrossRef](#)]
47. Alexander, M.R.; Thompson, G.E.; Beamson, G. Characterization of the Oxide/Hydroxide Surface of Aluminum Using X-Ray Photoelectron Spectroscopy: A Procedure for Curve Fitting the O 1s Core Level. *Surf. Interface Anal.* **2000**, *29*, 468–477. [[CrossRef](#)]
48. Zähr, J.; Oswald, S.; Türpe, M.; Ullrich, H.J.; Füssel, U. Characterisation of Oxide and Hydroxide Layers on Technical Aluminum Materials Using XPS. *Vacuum* **2012**, *86*, 1216–1219. [[CrossRef](#)]
49. Do, B.P.H.; Nguyen, B.D.; Nguyen, H.D.; Nguyen, P.T. Synthesis of Magnetic Composite Nanoparticles Enveloped in Copolymers Specified for Scale Inhibition Application. *Adv. Nat. Sci. Nanosci. Nanotechnol.* **2013**, *4*, 045016. [[CrossRef](#)]
50. Gupta, R.; Pancholi, K.; Sa, R.D.E.; Murray, D.; Huo, D.; Droubi, G.; White, M.; Njuguna, J. Effect of Oleic Acid Coating of Iron Oxide Nanoparticles on Properties of Magnetic Polyamide-6 Nanocomposite. *JOM* **2019**, *71*, 3119–3128. [[CrossRef](#)]
51. Okhrimenko, D.V.; Nielsen, C.F.; Lakshtanov, L.Z.; Dalby, K.N.; Johansson, D.B.; Solvang, M.; Deubener, J.; Stipp, S.L.S. Surface Reactivity and Dissolution Properties of Alumina-Silica Glasses and Fibers. *ACS Appl. Mater. Interfaces* **2020**, *12*, 36740–36754. [[CrossRef](#)] [[PubMed](#)]
52. Hoque, E.; DeRose, J.A.; Bhushan, B.; Mathieu, H.J. Self-Assembled Monolayers on Aluminum and Copper Oxide Surfaces: Surface and Interface Characteristics, Nanotribological Properties, and Chemical Stability. *Appl. Scanning Probe Methods IX* **2007**, *111*, 235–281. [[CrossRef](#)]
53. Queffélec, C.; Petit, M.; Janvier, P.; Knight, D.A.; Bujoli, B. Surface Modification Using Phosphonic Acids and Esters. *Chem. Rev.* **2012**, *112*, 3777–3807. [[CrossRef](#)] [[PubMed](#)]
54. Gouzman, I.; Dubey, M.; Carolus, M.D.; Schwartz, J.; Bernasek, S.L. Monolayer vs. Multilayer Self-Assembled Alkylphosphonate Films: X-Ray Photoelectron Spectroscopy Studies. *Surf. Sci.* **2006**, *600*, 773–781. [[CrossRef](#)]
55. Hoque, E.; Derose, J.A.; Kulik, G.; Hoffmann, P.; Mathieu, H.J.; Bhushan, B. Alkylphosphonate Modified Aluminum Oxide Surfaces. *J. Phys. Chem. B* **2006**, *110*, 10855–10861. [[CrossRef](#)] [[PubMed](#)]
56. Bayer, B.C.; Fouquet, M.; Blume, R.; Wirth, C.T.; Weatherup, R.S.; Ogata, K.; Knop-Gericke, A.; Schlögl, R.; Hofmann, S.; Robertson, J. Co-Catalytic Solid-State Reduction Applied to Carbon Nanotube Growth. *J. Phys. Chem. C* **2012**, *116*, 1107–1113. [[CrossRef](#)]